JMEPEG
https://doi.org/10.1007/s11665-022-07084-w

1059-9495/$19.00

TECHNICAL ARTICLE

Laser Additive Manufacturing Process Development for Bismuth Telluride Thermoelectric Material

Haidong Zhang and Saniya LeBlanc

Submitted: 22 September 2021 / Revised: 30 May 2022 / Accepted: 12 June 2022

Thermoelectric generators have strong potential for aerospace and aircraft applications. However, traditional manufacturing methods for thermoelectric devices severely limit device adaptability and consequently marketability. Laser powder bed fusion is an additive manufacturing method which shows promising potential for producing thermoelectric devices. Thermoelectric materials pose unique challenges compared to metals because of low thermal conductivity, brittle fracture characteristics, and irregular powder particle morphologies. Herein, we communicate processing procedures to fabricate thermoelectric parts of Bi_2Te_3 through laser powder bed fusion. We identify the successful combination of key process parameters—laser power, scan speed, hatch distance, and powder layer thickness—to achieve high-quality parts in terms of density and physical properties, and we demonstrate the impact of process parameter variation on built part quality. While it cannot exclusively determine part quality, the volumetric energy density is a useful guide in deciding process parameters for thermoelectric materials, and the optimal value is between 9 and 11 J/mm^3 for Bi_2Te_3. We demonstrate successful fabrication of different freeform geometries of Bi_2Te_3 powders. The results suggest it is possible to extend this method more broadly to other semiconductor materials, including thermoelectric power generation materials applicable for space applications.

Keywords additive manufacturing, bismuth telluride, laser powder bed fusion, selective laser melting, thermoelectric materials

1. Introduction

Onboard power generation for space exploration vehicles is a pressing issue. Radioisotope thermoelectric generators have been used for decades to power space vehicles because thermoelectric generators provide a reliable power source over long times (Ref 1). Thermoelectric semiconductor devices have unique advantages for thermal to electrical energy conversion. As heat engines, thermoelectric generators can directly generate electricity from waste heat; on the other hand, thermoelectric coolers provide solid-state cooling through the Peltier effect. Both thermoelectric generators and coolers have no mechanically moving parts, so they are more compact than alternative power generation (such as photovoltaic panels) and standard refrigeration systems. In spite of these advantages, thermoelectric devices have failed to become widespread in energy efficiency and thermal management applications, in part because the manufacturing process limits device design and adaptability. As the space exploration community turns to metal additive manufacturing in order to reach design goals (e.g., lightweight parts, increased complexity, low volume manufacturing), it will be necessary to consider how power generation can be integrated into the structural components made via metal additive manufacturing. The work discussed in this manuscript will report on how thermoelectric components can be made using a common metal additive manufacturing process, thus offering potential for integration of thermoelectric material and traditional structural materials into vehicle design using additive manufacturing.

Traditionally, thermoelectric device manufacturing involves a series of processing steps such as hot pressing, dicing, polishing, metallization, brazing, and assembly (Ref 2). The lengthy process inevitably leads to low production rate, limited yield, and high cost. For example, thermoelectric materials are typically expensive because they must be high purity and sometimes require rare earth elements, and the ingot dicing step wastes approximately 50% of this high-value material. More importantly, the traditional fabrication technique does not provide any capability to adapt the device geometry for optimal performance or system integration. Most thermoelectric units are made as cuboids because it is challenging to produce crack-free parts of any other shape with the current manufacturing approach. These limitations hinder the development of thermoelectric devices with broad applicability.

Laser powder bed fusion (L-PBF) (also known as selective laser melting and direct metal laser sintering) is an additive manufacturing technique used to build bulk structures in a

This invited article is part of a special issue in the *Journal of Materials Engineering and Performance* entitled "Space and Aerospace Exploration Revolution: Metal Additive Manufacturing." The issue was organized by Shahrooz Nafisi, Relativity Space; Paul Gradl, NASA Marshall Space Flight Center; Douglas Hofmann, NASA Jet Propulsion Laboratory/California Institute of Technology; and Reza Ghomashchi, The University of Adelaide, Australia.

Haidong Zhang and **Saniya LeBlanc**, Department of Mechanical & Aerospace Engineering, The George Washington University, Washington, DC 20052. Contact e-mails: haidongzhang@gmail.com sleblanc@gwu.edu.

Published online: 27 June 2022

layer-by-layer fashion. It offers unprecedented possibilities for quickly producing lower cost, freeform, 3D parts. Additive manufacturing has been applied to several material families, including metals/alloys (Ref 3), polymers (Ref 4), and ceramics (Ref 5). Recently, the L-PBF technique has also been attempted on semiconductor thermoelectric materials, both in powder and ink/slurry form. El-Desouky et al. demonstrated it was possible to laser melt bismuth telluride (Bi_2Te_3) powders (Ref 6) and investigated single melt lines (2016) (Ref 7) and the microstructures therein (2017) (Ref 8). Zhang et al. first realized successful L-PBF processing on loose powders of Bi_2Te_3 thermoelectric materials to form a bulk device without any pre- or post-processing (Ref 9). Carter et al. investigated the narrow process window for applying pulsed laser melting to thermoelectric materials (Ref 10). Wu et al. demonstrated dispenser printing combined with L-PBF on Bi_2Te_3-based slurry (Ref 11). Mao et al. studied the L-PBF processing window of Bi_2Te_3-based slurry (Ref 12), and Kim et al. demonstrated extrusion-based 3D printing on Bi_2Te_3-based inks (Ref 13). Slurry-based L-PBF requires development of suitable inks and an annealing post-processing step. By contrast, the powder-based method is a one-step process, enables direct-build of 3D shapes, and conforms to prevalent, industrial L-PBF practices.

Although there are many detailed studies for L-PBF on metals or ceramics, L-PBF on thermoelectric materials is a relatively new endeavor, so many aspects of the process still require exploration. In this work, we communicate the laser fabrication and process parameters for Bi_2Te_3 powders. Bi_2Te_3 is a typical thermoelectric semiconductor material; Bi_2Te_3 and its alloys have been the most common materials for thermoelectric applications in low temperature ranges (Ref 14). Here, we demonstrate successful additive processing of Bi_2Te_3 powders with L-PBF to form bulk, 3D structures (including geometries which are not achieved through the traditional manufacturing approach).

2. Laser Processing Experiments

2.1 Methods

Bi_2Te_3 dry powder (99.98% trace metal basis, Alfa Aesar) was sieved (−270 mesh) to isolate particles smaller than 53 μm in size (Fig. 1). This semiconductor material has a thermal conductivity of 3 W/(m·K) at 300 K and a melting point of 858 K (Ref 15). The electrical resistivity for a hot-pressed ingot made from this powder is about 0.6 mΩ·cm (Ref 9).

The uncharacteristic properties of thermoelectric material powders create unique challenges for their processing via L-PBF. For example, spreading powder layers is more difficult for thermoelectric materials than for the more common metals or alloys. Metallic powders used in L-PBF have particles with spherical morphology, but the morphology of thermoelectric powder particles is highly irregular. A comparison of the particle morphology for typical stainless steel powders and the Bi_2Te_3 powders which are used in this work is shown in Fig. 1. Unlike spherical powders, irregularly shaped particles can result in mechanical interlocking during the spreading process. As a result, the "flowability" for thermoelectric powders is generally worse than that for metals, and, consequently, the powder bed density and surface flatness are usually different. The Bi_2Te_3 powder employed in this work frequently formed clumps, inhibiting powder flow.

The angle of repose was measured for both the Bi_2Te_3 and the stainless steel powders using the fixed funnel method (Ref 16). A photograph of the newly formed powder pyramid was taken. Using an image processing software (FIJI), the angle between the top horizon, the top of the point, and the bottom corner, was measured. Each of these measurements was taken five times per trial, for a total of five trials. For each trial, the powder previously used was put back into the vial it came from and mixed with the powder stock in the vial. This mixing helps reduce error associated with smaller diameter particles settling to the bottom of the vial and thus being disproportionately underrepresented in the measurement. All measurements were conducted in a fume hood.

The average angle of repose for this powder was 50.67 ± 1.74 degrees (Fig. 2a), which suggests poor or "cohesive" flowability, according to the Carr classification of flowability (Ref 16). By comparison, the stainless steel powder had an average angle of repose of 34.97 ± 0.97 which indicates good or "free" flowability (Ref 16), and, indeed, that powder flowed smoothly (Fig. 2b). Furthermore, the thermal conductivity (and thus thermal dissipation) is higher in metals than in thermoelectric materials. The powder bed properties and the light–matter interactions are very different when comparing thermoelectric, metallic, and ceramic materials. For example, the powder layer thickness of thermoelectric materials (here 100-150 μm for Bi_2Te_3) may be much greater than that for metals. For instance, Wang et al. (Ref 17) employed 17 μm and 30 μm for particle size and layer thickness for 316L stainless steel, respectively. So, the process parameters which are

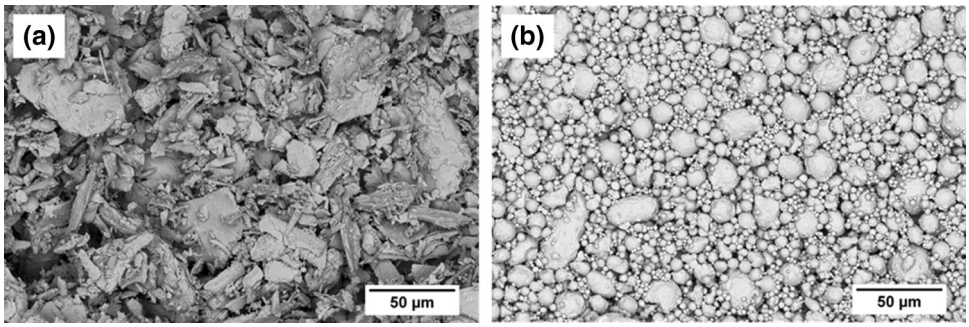

Fig. 1 A scanning electron micrograph comparison of particle morphologies used in laser powder bed fusion process. (a) A commercial Bi_2Te_3 powder which has been separated through a -270 mesh (53 μm) sieve. (b) Stainless steel SS340 atomized powder

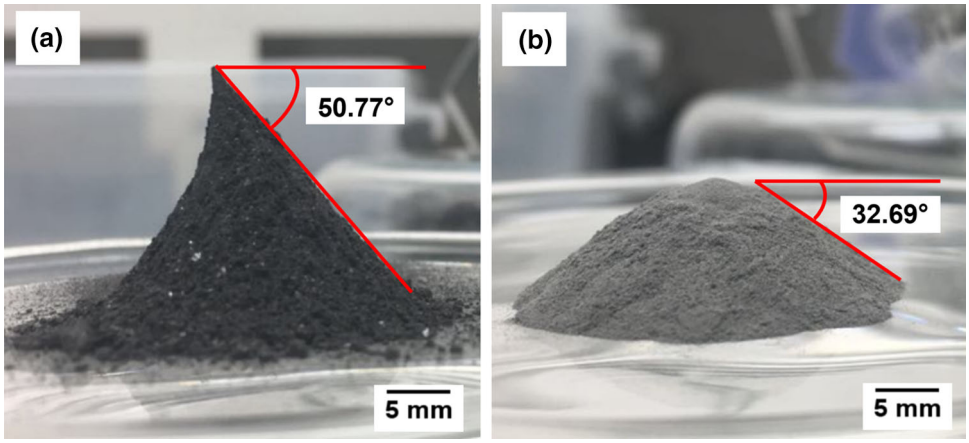

Fig. 2 Angle of repose for (a) a commercial Bi_2Te_3 powder which has been separated through a −270 mesh (53 μm) sieve. (b) a standard stainless steel SS340 atomized powder

suitable for metals [e.g., laser wavelength 1.09 μm, power 150 W for 316L stainless steel (Ref 17)] or ceramics [e.g., laser wavelength 10.6 μm, power 120 W for silica sand (Ref 18, 19)] may be different, sometimes by a large amount, for thermoelectric materials [e.g., laser wavelength of 1.07 μm, laser power 30 W for half-Heusler material ZrNiSn (Ref 20)].

Our L-PBF experiments were conducted with a custom-built L-PBF system since no commercial systems were designed to work with thermoelectric materials. The overall system consists of three main parts: laser system, power bed platform, and oxygen-deficit environment. The laser system controls the laser spot for accurate movements in a 2-D horizontal plane with the adjustable power, speed, movement mode, etc. The powder bed platform enables powder spread and formation of a flat powder layer with desirable thickness. The platform also adjusts the powder bed vertically after completion of one laser scan to guarantee the height of each new powder layer is identical during the whole process. The laser head and the powder bed platform are completely enclosed inside a laser welding enclosure which is filled with inert gas to form an oxygen-deficient environment. This custom-built system allows substantial flexibility for a wide variety of powder materials, large ranges of process parameters, and ease of future upgrades and modifications. A schematic of the L-PBF process and the experimental setup are shown in Fig. 3.

The powder was spread onto the build platform to form a thin, flat surface. The layer thickness was controlled by a manually actuated Mitutoyo micrometer with a resolution of 10 μm which was sufficient for the targeted layer thickness of 100 to 150 μm. A 1070 nm laser (IPG Photonics, YLR-series fiber laser, equipped with a mid-power scanner) was scanned over the powder surface following a pre-designed pattern composed of vectors paths. The diode-pumped Ytterbium fiber laser operated in CW mode with a power output up to 100 W. During the experiment, the laser spot size was focused to about 50 μm. At 300 K, the absorption coefficient α for a 1070 nm light is about 1.4×10^5 cm^{-1} for Bi_2Te_3, and the corresponding real and imaginary parts of the complex refractive index n and κ is about 6.7 and 5.9, respectively (Ref 21). It is noted that the L-PBF process enters high-temperature zone to form a melt pool and evaporate materials, and the optical properties will deviate from the values at room temperature. It is also known that the light absorption for a smooth bulk surface is usually much lower than a powder format due to the multiple reflections effect (Ref 22, 23). The laser energy was partially absorbed by the power bed, resulting in rapid melting and solidification of powder. A thin layer of Bi_2Te_3 was then solidified in the shape of the scanned pattern with the layer thickness in the range of 100 to 150 μm. Another layer of powder was spread, and the process was repeated. Using the layer-by-layer approach, an ingot of Bi_2Te_3 with desired shape and thickness was eventually fabricated. The unprocessed powders were collected and recycled. The L-PBF process was conducted in an inert gas (nitrogen or argon) environment with the oxygen level no greater than 4%. Even though commercial L-PBF is conducted with a lower threshold for the oxygen limit, no apparent oxidation was observed for the Bi_2Te_3 processing experiments as evidenced by the lack of oxide peaks in x-ray diffraction analysis (Ref 9). While oxygen level could impact transport properties, the process parameter exploration in this work targeted mechanical integrity of the final part. Initial investigations in which the oxygen level was below 0.5% showed no apparent difference in terms of part formation or surface roughness compared to parts made in the highest oxygen level of 4%. L-PBF-produced parts were assessed through a series of steps: visual evaluation of the surface condition, surface crack formation or propagation in response to handling, and density measurements. As reported elsewhere, the thermoelectric properties of parts that remained intact were characterized separately. The Bi_2Te_3 samples manufactured from different process parameters exhibited clear difference in mechanical strength. In response to a slight tapping from a sharp stainless steel tip, crack formation was observed in samples fabricated with process parameters that deviated from the optimal parameters. Therefore, a combination of the three steps provided sufficient information about the welding status and mechanical strength of the L-PBF-produced parts to determine the feasibility of subsequent transport property characterization.

In general, an L-PBF process can be affected by laser-, powder- and material-related factors (Ref 19, 24-26). Although many factors can influence the fusion process in a laser powder bed, laser and scanning parameters as well as powder layer thickness are among the most important ones. Selecting them appropriately critically affects the formation and properties of the fabricated part. Laser melting systems often have fixed

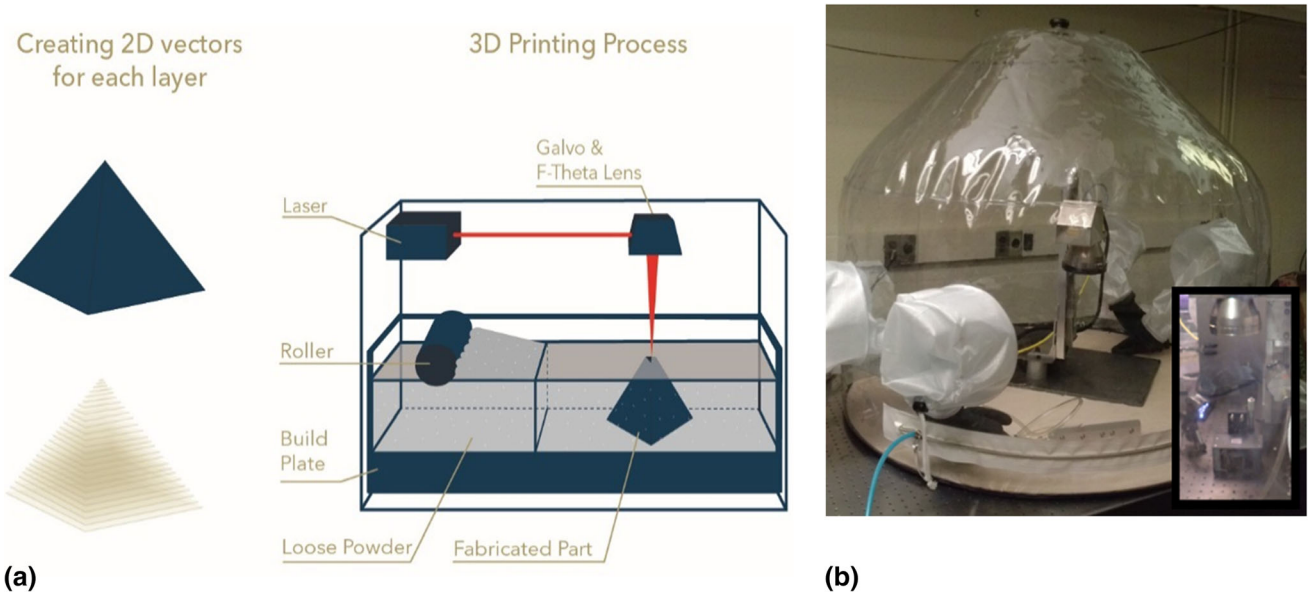

Fig. 3 (a) Schematic of the laser powder bed fusion process (known colloquially as 3D printing). (b) Custom-built L-PBF system for thermoelectric materials. The inset shows the powder spreading rig

operation mode (pulsed or continuous wave), light wavelength, and beam spot size. The adjustable laser processing parameters include laser power p, scan speed v, and hatch distance h (the distance between two neighboring melted lines). Isolating the appropriate laser and powder layer parameters is closely related to the complex light–matter interaction of converting optical energy to thermal energy at the powder bed. It is common practice to use one factor to represent the combined effect of all these parameters. There are several approaches to define such a factor. These include line energy (J/mm) (Ref 27),

$$E = \frac{p}{v} \quad \text{(Eq 1)}$$

laser energy density (J/mm^2) (Ref 28),

$$E = \frac{p}{vh} \quad \text{(Eq 2)}$$

volumetric energy density (J/mm^3) (Ref 29),

$$E = \frac{p}{vhd} \quad \text{(Eq 3)}$$

or another way of calculating volumetric energy density (J/mm^3) (Ref 30)

$$E = \frac{p}{v\sigma h} \quad \text{(Eq 4)}$$

where E is the respective energy density, d is the layer thickness, and σ is the laser spot diameter. The adoption of any method usually depends on the particular laser system and properties of materials. In this work, we use volumetric energy density Eq 3 (J/mm^3) to represent the overall influence from laser heating and powder layer properties. It has been suggested that the volumetric energy density (J/mm^3) is more accurate to describe energy intensity threshold or energy dose than the surface energy density (J/mm^2) in 3D printing of polymeric structures (Ref 31).

For the experiments, we used sieved particles of Bi_2Te_3 with the particle sizes below 53 μm (-270 mesh). The information for powder separation, selection, and particle size distribution can be found elsewhere (Ref 32), which confirmed that the majority of the particles are non-spherical with <53 μm nominal diameter, and the powder contained a large amount of particles with effective diameter below 10 μm. This size range balanced powder "flowability" and powder bed density. As shown in Fig. 1, Bi_2Te_3 powder consists of irregularly shaped particles which do not flow or spread as effectively as spherical particles due to mechanical interlocking between powder particles. In order to improve flowability, larger particle size is desirable because smaller ones have larger total surface and contact areas resulting in greater friction between the particles. However, larger powder particles result in voids in the powder bed, so packing density is low. A balance between these competing factors was achieved by using a sieved particle size below 53 μm as demonstrated in (Ref 32). In addition, this particle size is not greater than the laser spot size, which enables uniform melting. Because of the large particle size and low flowability of the Bi_2Te_3 powder, a layer thickness of 100-150 μm was achievable. Powder layers thinner than 100 μm with flat surfaces were more difficult to achieve because particles would protrude from the surface. Layers with 300 μm thickness were formed more easily (Ref 32), but the thickness was too large for light penetration or sufficient layer melting and fusion between layers. A layer thickness of 100-150 μm was used for Bi_2Te_3 processing described in this work, and further tuning of powder morphology and size distribution to enable thinner layers is a necessary step in the development of laser processing for thermoelectric materials.

2.2 Experimental Results

We used the L-PBF process described in Fig. 3 and adjusted the three laser processing parameters and the powder layer thickness to build 3D objects out of Bi_2Te_3. The results are shown in Fig. 4 where the x-axis is the laser power, and the y-axis is the hatch distance. Images with solid and blue frames (color online) represent a scan speed of 500 mm/s, and those with dotted and red frames represent a scan speed of 350 mm/s.

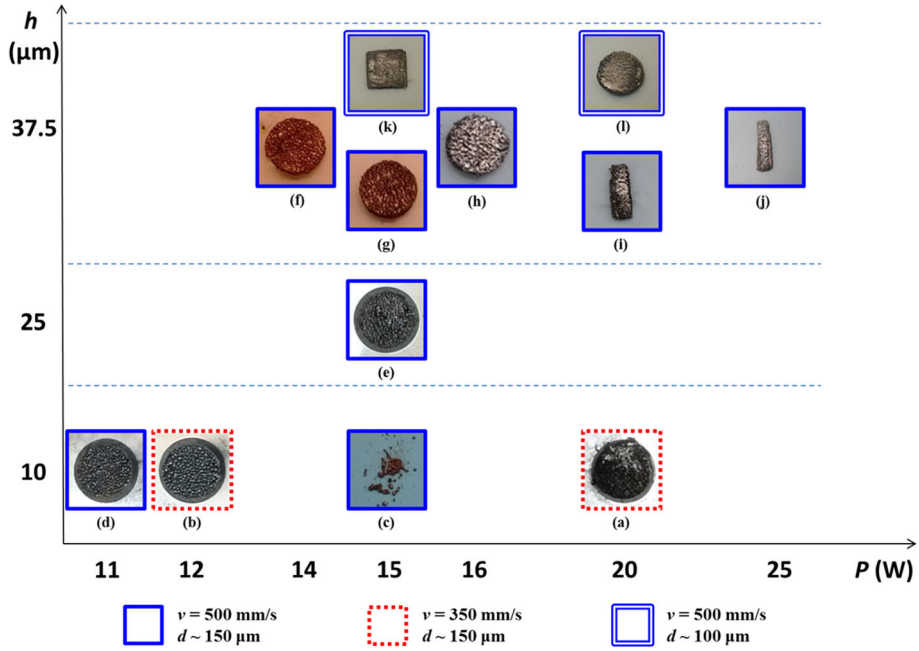

Fig. 4 Photographs of parts fabricated with different process parameters: (a)-(d) show the situation when excess photon energy was applied the powder bed; (e)-(i) and (k) show the situation when deficient laser energy was absorbed by the powder bed; (j) and (l) show the situation when laser parameters and power layer thickness are chosen close to the optimal values. (a)-(h) are disks with diameter of 8 mm; (i) and (j) are rectangular samples ~ 3 × 11 mm and ~ 3 × 14 mm, respectively. (k) is square with a side length of ~ 12 mm; (l) is a disk with diameter of ~ 12 mm (and is not to scale with the other disk images). All samples are thicker than 1 mm. In order to improve readability, the axes are not linearly scaled

Table 1 Laser processing parameters corresponding to Figure 4 for laser powder bed fusion of Bi_2Te_3

Bi_2Te_3	Power *p* (W)	Scan speed *v*, mm/s	Hatch distance *h*, μm	Layer thickness *d*, μm	Volumetric energy density *E*, J/mm^3	Inert gas environment
a	20	350	10	~150	~38	N_2
b	12	350	10	~150	~23	N_2
c	15	500	10	~150	~20	N_2
d	11	500	10	~150	~15	N_2
e	15	500	25	~150	~8	N_2
f	14	500	37.5	~150	~5	N_2
g	15	500	37.5	~150	~5	N_2
h	16	500	37.5	~150	~6	N_2
i	20	500	37.5	~150	~7	N_2
j	25	500	37.5	~150	~9	N_2
k	15	500	37.5	~100	~8	Ar
l	20	500	37.5	~100	~11	Ar

Laser power, scan speed, and hatch distance are nominal values from IPG Photonics

A single-line frame represents a layer thickness of ~150 μm, and a double-line frame represents a layer thickness of ~100 μm. The process parameters shown graphically with the images in Fig. 4 are also presented in tabular format in Table 1. Fig. 4(a)-(h) and (l) is disks, while Fig. 4(i) and (j) is rectangular, and Fig. 4(k) is square. Different shapes illustrate the advantage of the L-PBF process over the traditional thermoelectric part fabrication method since completely new tooling would be required to achieve different shapes with the traditional method. Excess or deficient laser energy density results in weak mechanical integrity in the L-PBF-produced Bi_2Te_3 parts. When excess photon energy was applied to the powder bed (Fig. 4a-d), balling phenomena were observed. This is illustrated in Fig. 4(c) where the sample readily shattered after gentle handling, and the original disk shape was not preserved. On the other hand, insufficient laser energy (Fig. 4e-i) led to inter-layer fusion but rough surfaces. Figure 4f shows this situation, and the sample cracked when light force was applied. The surface condition was only qualitatively evaluated because of the apparent roughness and mechanical weakness from those constructed using the suboptimal process parameters. When laser parameters are properly chosen, a mechanically stronger product with lower surface roughness can be achieved, as shown in Fig. 4(j) and (l). By comparison, a disk formed with a volumetric energy of 6 J/mm^3 shows a density of 6.27 g/cm^3, while a disk made with 9 J/mm^3 has a

density of 6.81 g/cm^3, causing an increase in relative density from 81 to 88% (Ref 9). Other samples formed with smaller volumetric energy (for example, ~ 5 J/mm^3, Fig. 4f and g) were less dense and had a propensity to crack. The overall best specimens were produced with the volumetric energy density in the mid-range, approximately 9 to 11 J/mm^3. Therefore, although the volumetric energy density E cannot be used as a quantitative measure, it can provide a useful guide in the L-PBF processing of Bi_2Ti_3 materials.

The samples that did not crack or fracture with handling were characterized for structure and physical properties (Ref 9). A scanning electron micrograph of a polished cross section is provided in Fig. 5 where no separation between powder layers was observed, but pores inside the L-PBF samples were evident (Ref 9). The thermoelectric properties of the intact Bi_2Ti_3 samples (for example, Fig. 4j) have been reported elsewhere (Ref 9) and show that laser processing alters the nanostructure such that thermoelectric properties change compared to traditionally formed thermoelectric parts. The temperature-dependent absolute Seebeck coefficient and electrical conductivity for the optimal L-PBF samples are reproduced in Fig. 6 (Ref 9). The thermal conductivity measurement and the figure of merit of the L-PBF-processed Bi_2Te_3 sample can be found elsewhere (Ref 9). The nano-structure of a similar L-PBF-processed $Bi_2Se_{0.3}Te_{2.7}$ sample shows nanoscale inclusions and highly textured columnar grains oriented in the build direction (Ref 33).

3. Discussion

Additively manufacturing thermoelectric devices is a relatively new endeavor, so it is critical to evaluate the influence of the process parameters on the L-PBF-produced thermoelectric parts. A analytical method based on a heat transfer model was developed to simulate the characteristics of the three-dimensional, transient melt pool due to L-PBF processing for thermoelectric Bi_2Te_3 powders (Ref 34). For the process parameters similar to the experiments (i.e., laser power of 20 W, scanning speed of 500 mm/s, and laser spot size of 50 μm), the predicted melt depth (100 μm) was in the same range of the powder layer thickness (~100-150 μm) used in experiments. Therefore, full melting through the thickness of the entire layer was predicted and experimentally supported. For high integrity processed parts, the maximum melt depth must be higher than the powder layer thickness to achieve complete layer melting and inter-layer fusion.

The process parameters have shown strong influence on the additively produced thermoelectric samples. The parts in Fig. 4(e) and (k) provide an interesting comparison. They were produced by similar volumetric energy density, but the resulting parts were different. The specimen in Fig. 4(k) has a slightly better surface quality and appears less porous than the one shown in Fig. 4(e). The processing differences between these two are a smaller hatch distance h for 4e and a smaller layer thickness d for 4k; the product (h•d) is the same for the two cases. This suggests that scanning parameters (e.g., hatch distance) and powder bed characteristics (e.g., layer thickness) have different influences on surface quality and overall sample quality although the two parameters appear to have the same influence when considering only the equation for volumetric energy density. The varied influence among the key laser factors was previously reported: laser power, hatch distance, and scan speed have different impacts on the mechanical bending strength, relative density, and sample morphology (Ref 35–37). Our experiment resulted in different products in 4e and 4k and thus demonstrated varied influence between hatch distance (laser factor) and layer thickness (powder bed factor). Therefore, the results on Bi_2Ti_3 thermoelectric materials compared the effect of one laser factor to one powder bed factor and concurred with the general conclusions that processing parameters do not necessarily influence the final parts equally in laser powder bed fusion. Because the volumetric energy density E cannot differentiate the influence of each

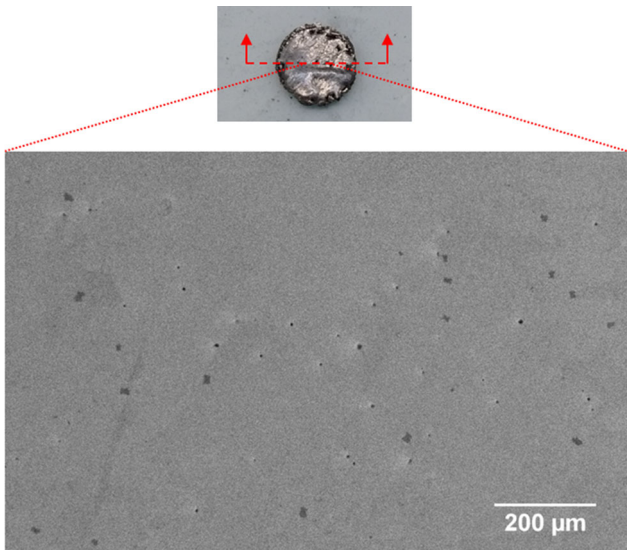

Fig. 5 Scanning electron micrograph of a polished cross section of the SLM processed Bi_2Te_3 bulk sample. Reprinted by permission from Springer Nature Customer Service Centre GmbH: Springer Nature, *Journal of Materials Research,* Laser additive manufacturing of powdered bismuth telluride, Haidong Zhang et al., Copyright 2018 (Ref 9)

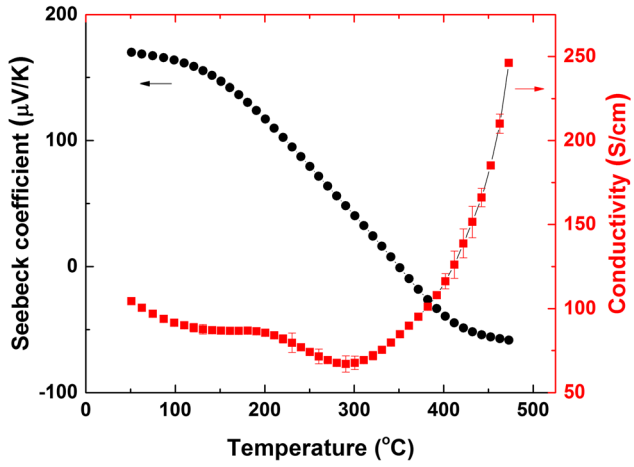

Fig. 6 The absolute Seebeck coefficient and electrical conductivity from 50 to 473 °C for the L-PBF-processed Bi_2Te_3 sample. Reprinted with permission from Springer Nature Customer Service Centre GmbH: Springer Nature, *Journal of Materials Research,* Laser additive manufacturing of powdered bismuth telluride, Haidong Zhang et al., Copyright 2018 (Ref 9)

parameter (p, v, h, or d), it is a useful guide but may not be a comprehensive metric for the laser powder bed fusion process.

The morphology of powder particles has significant influence on additively manufactured parts. For example, Yi et al. investigated the effect of the surface morphology of a solidified droplet on remelting between neighboring aluminum droplets; the outcome showed the surface morphology of solidified droplets can lead to cold lap pores due to the blocking effect of ripples and solidification angles on the fusion between droplets (Ref 38). Yi et al. studied hole-defects in soluble core-assisted aluminum droplet printing (Ref 39) and performed hybrid 3D metal printing via droplet deposition over soluble cores (Ref 40). This body of research suggested irregular morphology of the building block can directly obstruct the remelting process and lead to hole defects in the formed parts. Overall, the surface morphology of metal particle has shown important influence on the metallurgical bonding and fusion process.

The particle morphology of metal additive manufacturing has strong implications for the L-PBF process on thermoelectric materials. As shown in Fig. 1, the powder particles of the Bi_2Te_3 thermoelectric material have irregular shapes. This powder morphology leads to low flowability (Fig. 2) and is expected to have direct influence on pore formation during the remelting and fusion process. This work showed a relative density of 88%, and the cross section of the sample had hole defects even after optimizing the process parameters (Ref 9, 33). This result suggests higher relative density can be expected with spherical powder particle morphology as was demonstrated in metal additive manufacturing (Ref 38–40). Therefore, a uniform, spherical thermoelectric material particle should be ideal for the L-PBF process. However, it is challenging to achieve such powder morphology with thermoelectric materials. Typical routes to achieve spherical particle morphology are atomization and plasma spheroidization. There are unique and substantial hurdles to performing these processes on thermoelectric material powders. First, thermoelectric materials are quite expensive as they must be high purity, and they often contain at least one rare earth element. Processes such as atomization with specialized starting material form factors (e.g., wire spool) and low yield are prohibitively expensive, particularly for preliminary research. The same is true for plasma spheroidization, a relatively newer approach that accommodates powder starting material and results in high yield. Exploratory work to attempt plasma spheroidization on novel materials such as thermoelectric materials typically requires a significant research and development effort in and of itself—before a spheroidized powder can be produced to enable L-PBF.

A key challenge with traditional thermoelectric part manufacturing is the limitation on part geometry: parts are usually cylindrical ingots and/or cuboid legs. To illustrate the freeform advantage of the L-PBF process, an "S" shaped 3D part made of Bi_2Te_3 is presented in Fig. 7. The part is ~10 mm long and over 1 mm thick. This is a unique demonstration of using L-PBF on Bi_2Te_3 powders (or any thermoelectric material) to create a form factor other than typical shapes (square, round, or rectangular); this result experimentally confirmed the capability of L-PBF to fabricate thermoelectric parts of complex shapes with relatively high geometric accuracy directly from dry powders. If the same part were manufactured with the traditional fabrication process, it would require more time, and up to ~80% of the thermoelectric material would be lost. Notably, almost all the unmelted powders were recycled in the current study.

Fig. 7 An "S" shape part made of Bi_2Te_3 is made additively using laser powder bed fusion. The thickness of the specimen is greater than 1 mm

4. Conclusions

This work provides processing information to build thermoelectric Bi_2Te_3 material with the L-PBF process. Appropriate process parameter selection is crucial to control the melting and solidification processes that happen in the thin powder layers in a very short period of time. The work demonstrates unique features for L-PBF applied to thermoelectric semiconductor materials. First, dry powders can be processed directly, so this method completely avoids slurries and the post-process heating they necessitate. Second, the process study qualitatively shows how the choice of laser parameters and powder layer thickness crucially influences material consolidation. The four most influential parameters are laser power, scan speed, hatch distance, and powder layer thickness, and a set of parameters that enables successfully built macroscale parts are laser power of 25 W, scan speed of 500 mm/s, hatch distance of 37.5 μm, and powder layer thickness of 150 μm, for the non-spherical Bi_2Te_3 powder particles with the majority of the size below 53 μm used here. The L-PBF samples still had interior porosity with these process parameters. Although volumetric energy density E is not a comprehensive indicator of successful powder fusion, it does provide a useful guide and a rough processing range to fabricate thermoelectric parts via L-PBF. For Bi_2Te_3, the E corresponding to a successful fabrication is ~ 9 J/mm^3. The agreement between experimental and computational results increases and represents the current understanding of the temperature gradients present during L-PBF of thermoelectric materials. Unique geometries of thermoelectric parts have been achieved with a purely powder-based approach, suggesting there are a broad range of possible applications using this method.

The work presented here represents the current state of the art in advanced "3D printing" of Bi_2Te_3 thermoelectric powder materials through laser powder bed fusion. The results demonstrate laser-based additive manufacturing has credible potential to improve processing and fabricating thermoelectric materials and devices. Recent analysis suggests that changing the shape of thermoelectric units can result in better performance (Ref 41, 42). This work provides a practical method to manipulate and create novel thermoelectric leg geometries. Moreover, the successful processing of thermoelectric materials indicates the viability of expanding laser additive manufacturing to other semiconductor materials—and thus a broader range

of applications, including electronic and solid-state energy conversion devices.

Acknowledgments

This work was supported by the National Science Foundation (CAREER Award No. 1943104), Oak Ridge National Laboratory Manufacturing Demonstration Facility RAMP-UP (Subcontract 4000145175), Virginia Center for Innovative Technology (CRCF Award MF16-020-En), and GWU University Facilitating Fund. This material is based upon work supported by the U.S. Department of Energy's Office of Energy Efficiency and Renewable Energy (EERE) under the Advanced Manufacturing Office (Award Number DE-EE0009100). The authors thank Rachel Gray for the characterization of the powder angle of repose as well as assistance with equipment setup. The authors thank Panagiotis Rammos for discussions regarding the computational analysis of the melt pool. The scanning electron micrographs were acquired by H.Z. in the George Washington University Nanofabrication and Imaging Center.

References

1. R.L. Cataldo and G.L. Bennett, U.S. Space Radioisotope Power Systems and Applications: Past, Present and Future, *Radioisot. - Appl. Phys. Sci.*, 2011 https://doi.org/10.5772/23914
2. S. LeBlanc, Thermoelectric Generators: Linking Material Properties and Systems Engineering for Waste Heat Recovery Applications, *Sustain. Mater. Technol.*, 2014, **1–2**, p 26–35. https://doi.org/10.1016/J.SUSMAT.2014.11.002
3. D.D. Gu, W. Meiners, K. Wissenbach and R. Poprawe, Laser Additive Manufacturing of Metallic Components: Materials, Processes and Mechanisms, *Int. Mater. Rev.*, 2012, **57**(3), p 133–164. https://doi.org/10.1179/1743280411Y.0000000014
4. M. Schmid, A. Amado and K. Wegener, Materials Perspective of Polymers for Additive Manufacturing with Selective Laser Sintering, *J. Mater. Res.*, 2014, **29**(17), p 1824–1832. https://doi.org/10.1557/jmr.2014.138
5. A. Zocca, P. Colombo, C.M. Gomes and J. Günster, Additive Manufacturing of Ceramics: Issues, Potentialities, and Opportunities, *J. Am. Ceram. Soc.*, 2015, **98**(7), p 1983–2001. https://doi.org/10.1111/jace.13700
6. A. El-Desouky, A.L. Read, P.M. Bardet, M. Andre, and S. Leblanc, "Selective Laser Melting of a Bismuth Telluride Thermoelectric Materials," *Proc Solid Free Symp*, 2015, p 1043–1050
7. A. El-Desouky, M. Carter, M.A. Andre, P.M. Bardet and S. LeBlanc, Rapid Processing and Assembly of Semiconductor Thermoelectric Materials for Energy Conversion Devices, *Mater. Lett.*, 2016, **185**, p 598–602. https://doi.org/10.1016/J.MATLET.2016.07.152
8. A. El-Desouky, M. Carter, M. Mahmoudi, A. Elwany and S. LeBlanc, Influences of Energy Density on Microstructure and Consolidation of Selective Laser Melted Bismuth Telluride Thermoelectric Powder, *J. Manuf. Process.*, 2017, **25**, p 411–417. https://doi.org/10.1016/J.JMAPRO.2016.12.008
9. H. Zhang, D. Hobbis, G.S. Nolas and S. LeBlanc, Laser Additive Manufacturing of Powdered Bismuth Telluride, *J. Mater. Res.*, 2018, **33**(23), p 4031–4039. https://doi.org/10.1557/jmr.2018.390
10. M.J. Carter, A. El-Desouky, M.A. Andre, P. Bardet and S. LeBlanc, Pulsed Laser Melting of Bismuth Telluride Thermoelectric Materials, *J. Manuf. Process.*, 2019, **43**, p 35–46. https://doi.org/10.1016/J.JMAPRO.2019.04.021
11. K. Wu, Y. Yan, J. Zhang, Y. Mao, H. Xie, J. Yang, Q. Zhang, C. Uher and X. Tang, Preparation of N-Type Bi_2Te_3 Thermoelectric Materials by Non-Contact Dispenser Printing Combined with Selective Laser Melting, *Phys. Status Solidi - Rapid Res. Lett.*, 2017, **11**(6), p 1700067. https://doi.org/10.1002/pssr.201700067
12. Y. Mao, Y. Yan, K. Wu, H. Xie, Z. Xiu, J. Yang, Q. Zhang, C. Uher and X. Tang, Non-Equilibrium Synthesis and Characterization of n-Type $B_2Te_{2.7}Se_{0.3}$ Thermoelectric Material Prepared by Rapid Laser Melting and Solidification, *RSC Adv.*, 2017, **7**(35), p 21439–21445. https://doi.org/10.1039/C7RA02677C
13. F. Kim, B. Kwon, Y. Eom, J.E. Lee, S. Park, S. Jo, S.H. Park, B.-S. Kim, H.J. Im, M.H. Lee, T.S. Min, K.T. Kim, H.G. Chae, W.P. King and J.S. Son, 3D Printing of Shape-Conformable Thermoelectric Materials Using All-Inorganic Bi_2Te_3-Based Inks, *Nat. Energy*, 2018, **3**(4), p 301–309. https://doi.org/10.1038/s41560-017-0071-2
14. H. Goldsmid and H. Julian, Bismuth Telluride and Its Alloys as Materials for Thermoelectric Generation, *Materials (Basel).*, 2014, **7**(4), p 2577–2592. https://doi.org/10.3390/ma7042577
15. W.M. Haynes, *CRC Handbook of Chemistry and Physics, 95th Edition*, CRC Press, Boca Raton, 2014
16. H.M.B. Al-Hashemi and O.S.B. Al-Amoudi, A Review on the Angle of Repose of Granular Materials, *Powder Technol.*, Elsevier B.V., 2018, pp. 397–417
17. D. Wang, Y. Liu, Y. Yang and D. Xiao, Theoretical and Experimental Study on Surface Roughness of 316L Stainless Steel Metal Parts Obtained Through Selective Laser Melting, *Rapid Prototyp. J.*, 2016, **22**(4), p 706–716. https://doi.org/10.1108/RPJ-06-2015-0078
18. Y. Tang, J.Y.H. Fuh, H.T. Loh, Y.S. Wong and L. Lu, Direct Laser Sintering of a Silica Sand, *Mater. Des.*, 2003, **24**(8), p 623–629
19. H. Zhang and S. LeBlanc, Processing Parameters for Selective Laser Sintering or Melting of Oxide Ceramics, in *Additive Manufacturing of High-performance Metals and Alloys - Modeling and Optimization*, ed. by I. Shishkovsky, 1st ed., *IntechOpen*, 2018, p 89–124. https://doi.org/10.5772/intechopen.75832
20. H. Zhang, S. Wang, P. Taylor, J. Yang, and S. LeBlanc, Selective Laser Melting of Half-Heusler Thermoelectric Materials, in *Energy Harvesting and Storage: Materials, Devices, and Applications VIII*, ed. by N.K. Dhar, A.K. Dutta, and P. Balaya, *Proc. SPIE*, 2018, **10663**, 106630B. https://doi.org/10.1117/12.2306099
21. D.L. Greenaway and G. Harbeke, Band Structure of Bismuth Telluride, Bismuth Selenide and Their Respective Alloys, *J. Phys. Chem. Solids*, 1965, **26**(10), p 1585–1604
22. D.T. Pham, S.S. Dimov and P.V. Petkov, Laser Milling of Ceramic Components, *Int. J. Mach. Tools Manuf.*, 2007, **47**(3–4), p 618–626
23. J. Deckers, K. Shahzad, J. Vleugels and J.P. Kruth, Isostatic Pressing Assisted Indirect Selective Laser Sintering of Alumina Components, *Rapid Prototyp. J.*, 2012, **18**(5), p 409–419
24. S. Sun, M. Brandt, and M. Easton, Powder Bed Fusion Processes: An Overview, *Laser Addit. Manuf. Mater. Des. Technol. Appl.*, Woodhead Publishing, 2017, p 55–77
25. H. Shipley, D. McDonnell, M. Culleton, R. Coull, R. Lupoi, G. O'Donnell and D. Trimble, Optimisation of Process Parameters to Address Fundamental Challenges During Selective Laser Melting of Ti-6Al-4V: A Review, *Int. J. Mach. Tools Manuf.*, 2018, **128**, p 1–20
26. N. Ahmed, I. Barsoum, G. Haidemenopoulos and R.K.A. Al-Rub, Process Parameter Selection and Optimization of Laser Powder Bed Fusion for 316L Stainless Steel: A Review, *J. Manuf. Process.*, 2022, **75**, p 415–434
27. F.R. Liu, J.J. Zhao, Q. Zhang, C. He and J.M. Chen, Processing and Characterizations of 2%PF/silica Sand Core-Shell Composite Powders by Selective Laser Sintering with a Higher Transmittance Fiber Laser, *Int. J. Mach. Tools Manuf.*, 2012, **60**, p 52–58. https://doi.org/10.1016/J.IJMACHTOOLS.2012.05.003
28. H.C. Ho, I. Gibson and W. Cheung, Effects of Energy Density on Morphology and Properties of Selective Laser Sintered Polycarbonate, *J. Mater. Process. Technol.*, 1999, **89–90**, p 204–210. https://doi.org/10.1016/S0924-0136(99)00007-2
29. Y. Wu, J. Du, K.-L. Choy and L.L. Hench, Laser Densification of Alumina Powder Beds Generated Using Aerosol Assisted Spray Deposition, *J. Eur. Ceram. Soc.*, 2007, **27**(16), p 4727–4735. https://doi.org/10.1016/J.JEURCERAMSOC.2007.02.219
30. J. Ciurana, L. Hernandez and J. Delgado, Energy Density Analysis on Single Tracks Formed by Selective Laser Melting with CoCrMo Powder Material, *Int. J. Adv. Manuf. Technol.*, 2013, **68**(5–8), p 1103–1110. https://doi.org/10.1007/s00170-013-4902-4
31. E. Skliutas, M. Lebedevaite, E. Kabouraki, T. Baldacchini, J. Ostrauskaite, M. Vamvakaki, M. Farsari, S. Juodkazis and M. Malinauskas, Polymerization Mechanisms Initiated by Spatio-Temporally Confined Light, *Nanophotonics*, 2021, **10**(2), p 1211–1242. https://doi.org/10.1515/NANOPH-2020-0551/ASSET/GRAPHIC/J_NANOPH-2020-0551_FIG_006.JPG

32. N. Batista, A. El-Desouky, J. Crandall, S. Wang, J. Yang, and S. LeBlanc, Powder Metallurgy Characterization of Thermoelectric Materials for Selective Laser Melting, *Informatics, Electronics and Microsystems TechConnect Briefs*, 2017, p 166–169
33. R. Welch, D. Hobbis, A.J. Birnbaum, G. Nolas and S. LeBlanc, Nano- and Micro-Structures Formed During Laser Processing of Selenium Doped Bismuth Telluride, *Adv. Mater. Interf.*, 2021, **8**(15), p 2100185. https://doi.org/10.1002/ADMI.202100185
34. P. Rammos, Numerical Framework for Selective Laser Melting Processing of Thermoelectric Materials, The George Washington University, 2020. https://scholarspace.library.gwu.edu/etd/v118rf25g
35. J. Liu, B. Zhang, C. Yan and Y. Shi, The Effect of Processing Parameters on Characteristics of Selective Laser Sintering Dental Glass-Ceramic Powder, *Rapid Prototyp. J.*, 2010, **16**(2), p 138–145. https://doi.org/10.1108/13552541011025861
36. U.S. Bertoli, A.J. Wolfer, M.J. Matthews, J.-P.R. Delplanque and J.M. Schoenung, On the Limitations of Volumetric Energy Density as a Design Parameter for Selective Laser Melting, *Mater. Des.*, 2017, **113**, p 331–340. https://doi.org/10.1016/J.MATDES.2016.10.037
37. K.G. Prashanth, S. Scudino, T. Maity, J. Das and J. Eckert, Is the Energy Density a Reliable Parameter for Materials Synthesis by Selective Laser Melting?, *Mater. Res. Lett.*, 2017, **5**(6), p 386–390. https://doi.org/10.1080/21663831.2017.1299808
38. H. Yi, L. Qi, J. Luo, D. Zhang, H. Li and X. Hou, Effect of the Surface Morphology of Solidified Droplet on Remelting Between Neighboring Aluminum Droplets, *Int. J. Mach. Tools Manuf.*, 2018, **130–131**, p 1–11
39. H. Yi, L. Qi, J. Luo and N. Li, Hole-Defects in Soluble Core Assisted Aluminum Droplet Printing: Metallurgical Mechanisms and Elimination Methods, *Appl. Therm. Eng.*, 2019, **148**, p 1183–1193
40. H. Yi, L. Qi, J. Luo, D. Zhang and N. Li, Direct Fabrication of Metal Tubes with High-Quality Inner Surfaces Via Droplet Deposition Over Soluble Cores, *J. Mater. Process. Technol.*, 2019, **264**, p 145–154
41. Y. Thimont and S. LeBlanc, The Impact of Thermoelectric Leg Geometries on Thermal Resistance and Power Output, *J. Appl. Phys.*, 2019, **126**(9), p 095101. https://doi.org/10.1063/1.5115044
42. B. Şişik and S. LeBlanc, The influence of leg shape on thermoelectric performance under constant temperature and heat flux boundary conditions, *Front. Mater.*, 2020, **7**, p 389. https://doi.org/10.3389/fmats.2020.595955